Journal of Materials Research and Technology 27 (2023) 5533–5540

Contents lists available at ScienceDirect

Journal of Materials Research and Technology

journal homepage: www.elsevier.com/locate/jmrt

Investigations on the topography and micro-mechanical properties of polyvinyl alcohol thin-film composites reinforced with hardwood biocarbon particles

Mariem Zouari [a,b], Stefan G. Stanciu [c], Joseph Jakes [d], Laetitia Marrot [e], Efstathios Fiorentis [c], George A. Stanciu [c], David B. DeVallance [a,b,f,1,*]

[a] InnoRenew CoE, Livade 6a, 6310 Izola, Slovenia
[b] University of Primorska, Faculty of Mathematics Natural Sciences and Information Technologies, Muzejski Trg 2, 6000 Koper, Slovenia
[c] National University of Science and Technology POLITEHNICA Bucharest, Center for Microscopy-Microanalysis and Information Processing, 313 Splaiul Independentei Street, 060042 Bucharest, Romania
[d] Forest Biopolymers Science and Engineering, USDA Forest Service, Forest Products Laboratory, One Gifford Pinchot Drive Madison, 53726 WI, USA
[e] ZAG fire laboratory, Obrtna cona Logatec 35, 1370 Logatec, Slovenia
[f] West Virginia University, Division of Forestry and Natural Resources, 322 Evansdale Drive, Morgantown, 26505, WV, USA

ARTICLE INFO

Handling Editor. P.Y. Chen

Keywords:
PVA thin films
biocarbon
surface roughness
nanoindentation
Micro-mechanical properties

ABSTRACT

In this study, we investigated the impact on surface topography and micro-mechanical properties of polyvinyl alcohol (PVA) thin films when loaded with hardwood-derived biocarbon particles (BCP). The PVA/BCP composites were prepared with the conventional film casting method, after varying BCP concentrations of 6, 8, 10, 12, and 20 wt% were added to the PVA solution. Atomic force microscopy (AFM) investigations and nano-indentation tests were performed. The average roughness of the thin films increased with the increase in BCP content. The alternation between dark and light patterns observed in the AFM images showed an irregular surface topography with alternating high peaks and deep valleys. The skewness and kurtosis parameters showed that the different dispersion degrees of the BCP within the PVA matrix influenced the composites' surface roughness. The micro-mechanical properties of the thin film composites depended on the BCP type and concentration. Films reinforced with red oak-derived BCP had higher hardness and Young's modulus compared to films reinforced with willow SV1 and yellow-poplar BCP, which was attributed to the high carbon content and low ash content of red oak BCP. We argue that these results may be extrapolated to other types of BCP-reinforced thin films and can significantly contribute to enabling more efficient methods and protocols for reinforcing polymers with hardwood biocarbon.

1. Introduction

Polyvinyl alcohol (PVA) is a synthetic biodegradable thermoplastic polymer [1] that has the potential for use in many composite and packaging applications. PVA is water-soluble and has been widely produced since 1924, when it was synthesized for the first time by Herrmann and Haehnel [2] via saponification of polyvinyl acetate (PVAc) homopolymer. Currently, PVA is mainly produced after the conversion of PVAc under methanolysis reaction [1]. PVA has received particular attention owing to its exceptional features, such as thermal stability, hydro-solubility, lightweight, cost efficiency, and ease of manipulation [3]. Furthermore, PVA is non-toxic and biocompatible, which makes it valuable for food packaging [4] and a wide range of pharmaceutical and biotechnological applications [5]. Given the viscoelastic nature and film-forming ability of PVA, it was used in applications such as wound dressings [6], bio-sensors, micro-encapsulation, and drug delivery [7]. The use of PVA has also extended to the fabrication of coatings [8] and piezoresistive pressure sensors [9]. For use in packaging application, an

Abbreviations: PVA, polyvinyl alcohol; BCP, Biocarbon particles; AFM, atomic force microscopy; PVAc, polyvinyl acetate; Ra, average roughness; Rq, root mean square; Rsk, surface skewness; Rku, kurtosis coefficient; ROI, region of interest; H, hardness; E, Young's modulus.

* Corresponding author. College of Science and Technology, Commonwealth University, 401 North Fairview Street, Lock Haven, PA 17745, USA.
E-mail address: ddevallanc@commonwealthu.edu (D.B. DeVallance).
[1] Present address: College of Science and Technology, Commonwealth University, 401 North Fairview Street, Lock Haven, PA 17745, United States.

https://doi.org/10.1016/j.jmrt.2023.10.217
Received 1 May 2023; Accepted 22 October 2023
Available online 7 November 2023

enhanced mechanical performance is a key requirement to define the potential of the films composites.

Prior studies have explored various ways to reinforce PVA film composites to improve their mechanical resistance. For instance, carbon derivatives such as carbon nanotubes [10], graphene sheets [11], and biocarbon particles (BCP) [12] have been investigated as potential reinforcements for PVA. Biocarbon is the solid residue generated by the thermal conversion of organic biomass at a high temperature and oxygen-free atmosphere [13]. Biocarbon is more available and more cost-efficient to produce compared to other carbon derivatives [14]. The high performance of BCP in reinforcing composites is usually assigned to its large surface area and porous structure, the presence of surface functional groups, and the high carbon content that encourages bonding with polymeric matrices [15]. Numerous studies reported the enhancement of mechanical properties upon the incorporation of BCP in different polymeric matrices, such as polypropylene [16] and polylactic acid [17]. Nan et al. [12] reported that mixed wood-derived BCP reinforcement significantly improved the tensile modulus of PVA films by 129 %, 271 %, and 429 % for BCP loading of 2 wt%, 6 wt%, and 10 wt%, respectively. However, their results indicated that the addition of BCP reduced the tensile strength by 58 %, 75 %, and 81 %, respectively. In their study, however, they did not evaluate the micro-mechanical properties of the BCP or the composite film material. Mousa et al. [18] found that the incorporation of 3 wt% of bamboo-derived BCP resulted in a 70.2 % and 71.6 % increment in the tensile modulus and tensile strength of PVA films, respectively, compared to the neat PVA. Nonetheless, the improvement in the mechanical properties with the reinforcement was found to be limited. An increase in the filler's content over a threshold was observed to lead to an opposite effect, resulting in mechanical failure. For instance, Mousa et al. [18] observed a remarkable decline in the tensile strength when BCP content was further increased to 5 wt% and 10 wt% (21 % and 33 % decrement, respectively). This behaviour was assigned to the presence of BCP aggregates which lowered the interfacial filler-matrix bonding. However, the tensile modulus of the composites increased from 3.54 GPa at 3 wt% of BC to 4.16 GPa at 10 wt% BC loading. A deeper understanding of the nano and micro-mechanical features of thin films is needed to better understand how BCP loadings and properties (i.e., particle size and composition) affect the performance of the overall composite.

The mechanical, electrical, and thermal properties of thin films can also be influenced by their surface topography [19] which refers to the different irregularities and deviations that can be random or repetitive, including waviness, lays, and flows. The surface roughness of thin films can be affected by the composite's preparation method, filler's content and distribution, filler's particle size, and polymeric chain organization, and it can directly influence the technological value of the materials [20].

Prior research studied the surface roughness of thin films and addressed roughness's impact on the external properties of the composites. For instance, Rytöluoto et al. [21] reported that increased surface roughness of biaxially oriented polypropylene films was correlated with lower dielectric strength. Çaycı et al. [22] showed for Langmuir Blodgett thin films of porphyrins, that a larger surface area, which is equivalent to higher roughness, leads to an enhanced response in gas sensing applications in terms of resonance frequency change. Guen et al. [23] investigated the relationship between surface roughness and heat transfer capacity of silicon probes, and they found that the samples' thermal conductance decreased with the increase of surface roughness. Rough surfaces are also not favorable in the case of filtration and biological membranes because of rapid fouling problems [24]. In addition, surface roughness is usually involved in the formation of biofilm on a membrane by favoring the adhesion of microbes within the high peaks and deep valleys that represent a shelter for microorganisms [25].

Nan [26] investigated the efficiency of PVA/BCP thin films as piezoresistive pressure sensors and packaging films. During the research work, the effects of variable BCP loadings, particle size distribution, and wood species used for BCP preparation on the mechanical, thermal, and electrical properties of the composites were investigated. However, prior studies did not evaluate the surface roughness or micro-mechanical properties of PVA films loaded with BCPs. The aim of this study was to investigate the impact on surface topography and micro-mechanical properties of PVA thin films when loaded with BCPs.

This study follows up on the previous work [26], shedding light on the influence of BCP addition on the surface roughness and micro-mechanical features of the thin film composites. Specifically, PVA/BCP films were produced using BCP previously prepared by pyrolysis of three different hardwood precursors: red oak (*Quercus rubra*), willow SV1 (*Salix* × *dasyclados*), and yellow-poplar (*Liriodendron tulipifera*). These particular BCPs were selected given their use in prior research on piezoresistive sensor films and resulting high carbon content and lower ash content, as compared to other plant-based biochar. Additionally, these species are widely available as residuals from sawlog harvesting operations (e.g., red oak and yellow-poplar) and as biomass grown on marginal lands (e.g., willow) in the Appalachian Region of the United States. The effect of BCP on the structural and micro-mechanical characteristics of the composite thin films was investigated.

The objectives of this study were to.

(i) Investigate the effect of BCP content and original biomass type (wood species) on roughness parameters, hardness, and Young's modulus of PVA thin films.
(ii) Investigate the filler-matrix interaction in PVA/BCP thin films at the nanoscale.

2. Materials and methods

2.1. Materials

The BCP used for this study was selected from materials prepared using three different hardwood species (red oak, willow SV1, and yellow-poplar) by carbonization at 1000 °C for 1 h at a heating rate of 5 °C/min, as outlined by Nan [26]. Additional details related to the physio-chemical composition and the size analyses of the BCP samples is provided in Nan [26]. For the purpose of this study, the proximate, density, porosity, and particle size results in Nan [26] are summarized in Table 1.

Polyvinyl alcohol (PVA) in powdered crystals form (Acros Organics, MFCD-00081922) with an average molecular weight of 86,000 g/mol and degree of hydrolysis >99 % was purchased from Fisher Scientific (Waltham, Massachusetts, USA).

Table 1
Proximate composition and physical and particle size properties of the BCP used for PVA film reinforcement [26].

	Proximate Analysis			Physical Properties		Particle Size
Parameters	Volatiles, %	Ash, %	Fixed carbon, %	Density, g/cm^3	BET surface area, m^2/g	Mean size, μm
Red oak BCP	5.5	0.9	93.7	0.20	428.2	385.6
Willow SV1 BCP	10	4.7	85.3	0.12	624.3	495.1
Yellow-poplar BCP	7.8	1.7	90.4	0.14	526.4	258.2

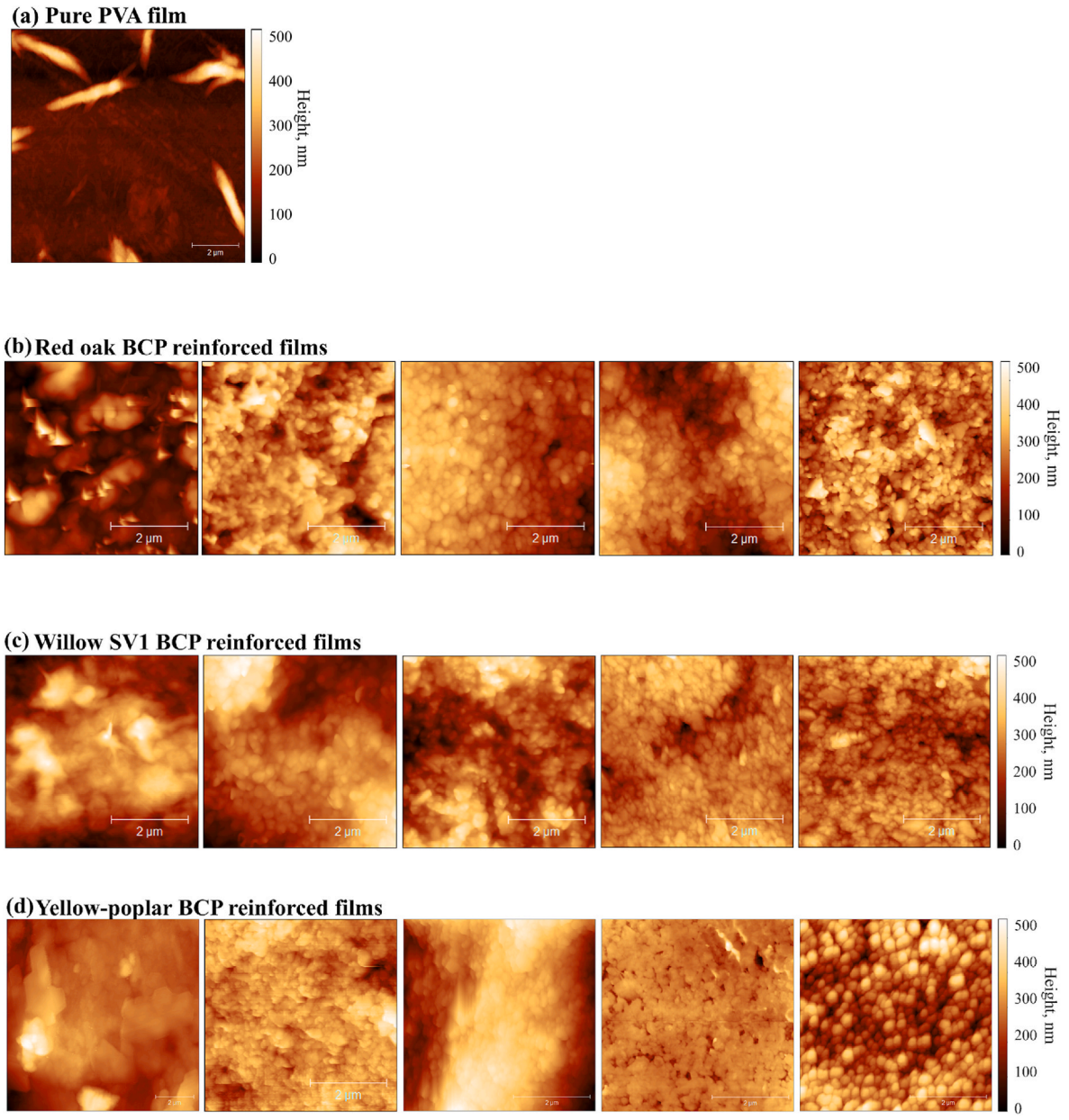

Fig. 1. Topographic 2D AFM images of PVA/BCP films (a) Pure PVA; films reinforced with (b) Red oak BCP; (c) Willow SV1 BCP, and (d) Yellow-poplar BCP. From left to right, BCP contents are 6, 8, 10, 12, and 20 wt%. Scale bars: 2 µm.

2.2. Film composites preparation

PVA/BCP films were prepared by introducing BCP with different loadings into aqueous PVA solutions. A 10 wt% PVA solution was prepared by adding PVA powder to the required amount of distilled water and heating it to up to 85 °C. The mixture was then continuously stirred on a magnetic stirrer at 85 °C until complete solubilization of the PVA. The obtained gel was allowed to cool down to room temperature and then stored at 4 °C until the preparation of the film.

BCP was added to the PVA solution at variable contents (0, 6, 8, 10, 12, and 20 wt%) to prepare the composites. During preparation, the solution with BCP was first mixed manually, followed by a 1 min ultrasonication (20 kHz, Model VCX 750, Sonics & Materials, Newtown, Connecticut, USA) at 50 % power to homogenize and distribute the BCP. Subsequently, the blends were cast by pouring the mixture into Petri dishes and degassing them under vacuum in a desiccator (60 Hz, Model 25,228–01, Welch, Mt Prospect, Illinois, USA) and left at ambient conditions (temperature of 25 °C and relative humidity of 30 %) until films formation. Finally, the films were oven-dried (Model 6524, Thermo Fisher Scientific, Waltham, Massachusetts, USA) at 55 °C for 6 h to obtain the composites with a final thickness of 0.5 mm ± 0.1 mm.

In total, 16 samples were obtained that consisted of the pure PVA reference and composites with five different BCP contents from three wood biomass types.

2.3. Characterization of the PVA/BCP thin films

An AFM system (NX10, Park Systems, Suwon, Korea) operated in non-contact mode was employed to investigate the surface topography of the synthesized samples. An aluminium-coated probe (PPP-NCHR 10 M, Nanosensors, Switzerland) with a radius of curvature <7 nm, and a tip length and width of 125 µm and 30 µm, respectively, were used. The resonant frequency of this probe was 330 kHz. The calibration of the equipment was carried out using an HS 100-MG probe (BudgetSensors,

Innovative Solutions Bulgaria, Ltd.) as a standard sample composed of silicon dioxide structure arrays on a 5 × 5 mm silicon chip. For each PVA/BCP sample, three images (256 × 256 pixels, 5 × 5 μm) were collected on different random regions of the surface using the Smart Scan software, proprietary to the NX10 AFM. Following data acquisition, the roughness parameters were calculated for all images using the open-source Gwyddion software [27].

Nanoindentation analysis was conducted using the same experimental setup used for AFM investigations. However, a specialized Sapphire cantilever with a diamond tip was utilized. The tip has the shape of a three-sided pyramid with a half angle of 30° and a radius of less than 25 nm. The length and thickness of the diamond tip were 1.045 μm and 34 μm, respectively, and the resonant frequency was 40 kHz. Before acquiring nanoindentation data, topography scans of a region of interest (ROI) were collected with the same probe, with the AFM system operated in contact mode. Three repetitions were performed for each sample formulation (One ROIs were investigated for each composite). Following this, force-displacement curves were acquired during the indentation (loading) with maximum depth set at 0.5 μm and retraction (unloading) of the indenter at x and y coordinates of the ROI imaged by AFM.

The method of Oliver and Pharr [28,29] was used to determine the micro-mechanical properties of the thin films. This method is based on the relationship between contact stiffness, the elastic modulus, and the contact area (Ac) [30]. The load-depth response was plotted, then hardness (H) and the Young's modulus (E) were calculated by linear fitting of the upper part of the unloading curves.

H is defined as the local resistance to plastic deformation [31] and is calculated from the ratio of applied load to the projected area as described in equation (1).

$$H = \frac{Pmax}{Ac} \tag{1}$$

where *Pmax* is the maximum load, and *Ac* is the area of contact between the indenter's tip and the sample's surface. *Ac* depends on the indenter's radius (*R*), the indenter's shape, and the indentation depth. It can be determined using equation (2).

$$Ac = 1.73 \times (hc - htip)^2 \tag{2}$$

where *htip* is the tip truncation used for *Ac* correction to get a geometrical idealization of the indenter. The *htip* was calculated considering a tip radius of 25 nm and was found to be equal to 17 nm.

The exact radius (r) value was calculated by considering the ideal geometry angle of the cantilever tip (α = 36.6°). Equation (3) was used.

$$r = htip \times \frac{sin\ \alpha}{1 - sin\ \alpha} \tag{3}$$

hc was determined from equation (4).

$$hc = hmax - 0.72 \times \frac{Pmax}{S} \tag{4}$$

where *hmax* describes the maximum penetration depth and *S* the initial slope of the unloading curve.

The reduced modulus (*Er*) and Young's modulus (*E*) were calculated using equations (5) and (6), respectively.

$$Er = \frac{\sqrt{\pi}}{2} \frac{S}{\sqrt{Ac}} \tag{5}$$

$$\frac{1}{Er} = \frac{1 - v^2}{E} + \frac{1 - vi^2}{Ei} \tag{6}$$

where *E* and *Ei* represent Young's modulus of the tested sample and the indenter, respectively, and *v* and *vi* are Poisson coefficients of PVA and the indenter, respectively. Empirical values for *Ei*, *vi*, and *v* are 1141 GPa, 0.07 [28], and 0.44 [32], respectively.

2.4. Statistical analysis

Data obtained were analyzed with NCSS software version 07.1.21. A significant difference in level was measured by one-way analysis of variance (ANOVA) at a 0.05 alpha level. Tukey-Kramer multiple comparison tests, as necessary, were applied to determine the differences among treated mean values. The differences generated by variation of the BCP contents and the biomass type were analyzed.

3. Results and discussion

In this section, the film samples are referred to using the first letter of the original biomass (R for red oak, W for willow SV1, and Y for yellow-poplar) followed by the BCP percentage (6, 8, 10, 12, and 20 wt%).

3.1. Atomic force microscopy (AFM) analysis

Fig. 1 displays topographic 2D AFM images of the pure PVA and PVA/BCP composite films, acquired for sample regions of 5 μm × 5 μm. The 3D AFM images are provided in the supporting information (Fig. S1).

The morphologies of PVA/BCP films differ from the pure PVA (Fig. 1a). For the non-reinforced PVA sample, the topography shows a flat surface (parts with homogeneous color) with the presence of a few random rod-shaped peaks distributed throughout the composite. The detected irregularity can be attributed to PVA clusters that originate from the poor solubilization of PVA crystals during the manufacturing process.

Upon addition of BCP, drastic changes occurred in the topography, with the surface of all PVA/BCP samples exhibiting a granular structure, as observed in the AFM images depicted in Fig. 1. As a rule of thumb for standard colormaps in AFM imaging, the dark parts of the AFM images represent deep valleys, whereas the brightest parts represent high peaks. The peaks that can be observed in Fig. 1b–d are attributed to the presence of BCP within the polymeric matrix, which changed the undulation of the surface and therefore affected the arrangement of PVA chains on the composite's surface.

Ali et al. [33] studied the changes in the surface nano-structure of PVA films loaded with variable concentrations of BiI3 nanoparticles (from 0 to 18.5 wt%) using AFM and observed that the surface morphology of doped PVA was characterized by the presence of mixed grains and colors caused by the presence of the BiI3 crystallites. Similar observations were reported in previous literature [34], where the surface topography of nano-sized poly (diaminonaphthalene)/PVA films were studied. Voss et al. [35] studied the surface morphology of an elastomeric polypropylene matrix using AFM in peak-force tapping mode, and they concluded that the changes in the dark-light ratio are the result of the presence of crystalline inhomogeneities at the nanoscale. Moreover, they stated that non-homogeneous regions could appear on the surface due to phase separation between short and long polymer chains during the composite preparation. Based on these previous findings, we speculate that the color differences that can be observed in Fig. 1 b-d can be potentially associated with the alternation between crystalline and amorphous phases, which characterize semicrystalline materials such as PVA.

The AFM images were used to extract a series of roughness parameters that are typically used to quantitatively assess the surface topography of a specimen (Table 2). The average roughness (Ra) describes the values of the average heights and depths across the surface, while the root means square roughness (Rq) indicates the root mean square along the length of the imaged surface. Surface skewness (Rsk) is a measure that describes the average of the first derivative of the surface (amount of symmetry loss). A negative value of Rsk indicates the dominance of valleys on the surface, while a positive skewness indicates that the surface is mainly composed of peaks. Finally, kurtosis (Rku) is a complementary parameter that helps to understand the shape of the peaks and valleys on the surface (i.e., sharpness or roundness).

Table 2
Surface roughness parameters extracted from AFM images of PVA and PVA/BCP films.

Samples	[a]Ra, nm	[b]Rq, nm	[c]Rsk	[d]Rku
Pure PVA	26 ± 5	40 ± 4	1.89 ± 0.72	4.44 ± 3.08
R-6%	164 ± 64	207 ± 81	−0.64 ± 0.28	0.03 ± 0.24
R-8%	61 ± 43	78 ± 56	−0,21 ± 0.51	0.17 ± 1.07
R-10 %	40 ± 14	51 ± 17	0.09 ± 0.14	−0.04 ± 0.19
R-12 %	136 ± 37	171 ± 51	−0.24 ± 0.60	−0.52 ± 0.26
R-20 %	54 ± 9	67 ± 11	0.02 ± 0.05	−0.25 ± 0.21
W-6%	59 ± 26	73 ± 30	−0.06 ± 0.21	−0.60 ± 0.16
W-8%	91 ± 54	65 ± 33	−0.19 ± 0.33	−0.78 ± 0.37
W-10 %	117 ± 46	146 ± 58	0.24 ± 0.50	−0.37 ± 0.59
W-12 %	179 ± 152	216 ± 177	0.11 ± 0.52	−0.48 ± 0.34
W-20 %	247 ± 200	295 ± 226	0.18 ± 0.50	−0.51 ± 0.74
Y-6%	55 ± 34	73 ± 41	−0.75 ± 0.60	1.01 ± 1.73
Y-8%	77 ± 27	97 ± 30	−0.27 ± 0.11	−0.29 ± 0.34
Y-10 %	252 ± 133	317 ± 148	−0.39 ± 0.28	−0.61 ± 0.09
Y-12 %	58 ± 25	85 ± 39	0.39 ± 0.08	0.35 ± 0.46
Y-20 %	42 ± 19	51 ± 23	0.10 ± 0.15	−0.40 ± 0.19

[a] Ra: average roughness.
[b] Rq: root mean square roughness.
[c] Rsk: surface skewness; and.
[d] Rku: kurtosis coefficient.

For the specimens reinforced with willow SV1-derived BCP, the Ra constantly increased from 59 ± 26 nm to 247 ± 200 nm upon increasing the BCP loading from 6 wt% to 20 wt% respectively, which is likely due to the increase in the number of the grains on the films' surface, which can be observed in the AFM images presented in Fig. 1c. However, for the specimens reinforced with red oak and yellow-poplar-derived BCP, both Ra and Rq varied in a non-typical way, with no correlation being observed between the BCP content and the Ra and Rq values, which increased then decreased anomalously. These observations are most likely a result of differences in the proximate composition of the BCP derived from the three wood species (Table 1); specifically, the higher ash content of willow SV1-derived BCP (4.7 %) compared to BCP prepared from red oak and yellow-poplar (0.9 % and 1.7 %, respectively). Ash components likely favor the homogeneous distribution of BCP over the films' surfaces by preventing the BCP from clustering. Due to the homogeneous distribution of the BCP, the surface roughness was comparable on the different surface areas of the investigated films, and the change of roughness values with the BCP percentage was linear. However, in the case of BCP with lower ash content (i.e., red oak and yellow-poplar BCP), the agglomeration of carbon particles was likely to happen more frequently. Therefore, the occurrence of aggregates resulted in heterogeneous regions on the thin films' surfaces, which was reflected by the non-proportional variation of Ra and Rq values with an increase in the BCP loadings. Choudhary and Sengwa [20] characterized the morphology of films made of binary blends (50:50 wt%) of PVA and poly (vinyl pyrrolidone) and mixed with ZnO nanoparticles (0, 1, 3, and 5 wt %). They found that the composites' roughness fluctuated anomalously with the increase of nano-sized ZnO content, which was assigned to the differences in particle distribution homogeneity.

Moreover, the abnormal trends in Ra fluctuation can be assigned to the different particle size distributions of the three BCP types (Table 1). Willow SV1-derived BCP has the highest mean size (495.1 μm) as compared to the red oak and yellow-poplar-derived BCP (385.6 μm and 258.2 μm, respectively). The larger particle size of BCP likely contributed to higher Ra that increased proportionally with the increase in particle loading. Furthermore, Ra and Rq variations can be assigned to the poor dispersion of the particles within the PVA polymeric matrix, as supported by the high standard deviations (Table 2). These high deviations of Ra and Rq values indicate that the cantilever tip was placed over areas with largely different structures when the test was conducted, i.e., areas with different BCP contents, which suggests an overall inhomogeneous surface of the synthesized thin films.

For the samples with negative Rsk, the surface topography is dominated by deep valleys, while for the samples with positive Rsk, the surface has more high peaks and asperities. In the case of our measurements, the Rsk varied between negative and positive values (Table 2), which aligns with the aspect of the AFM images in Fig. 1. It is worth mentioning that regardless of the original biomass, for higher BCP contents (10, 12, and 20 wt%), the Rsk values were higher, i.e., more peaks were present, which could be due to the occurrence of more aggregates due to the increase in BCP content. However, the Rku values varied between −0.61 ± 0.09 and 1.01 ± 1.73 and were negative and low for most of the samples except for pure PVA, which had a high Rku compared to reinforced films (4.44 ± 3.08). The remarkable changes in Rku upon BCP addition indicate that BCP presence directly affected the films' nano-structure. Similar findings were reported in a prior study [34] where pure PVA had a high Rku (79.17 ± 3.96) as compared to PVA films doped with diaminonaphthalene and poly (diaminonaphthalene) (−0.110 ± 0.004 and 2.62 ± 0.13, respectively). The dramatic decrement in surface Rku was assigned to the increase in the size of the dopant molecule and the doping extent. In the same study [34], kurtosis was found to depend on several factors, such as the thickness of the film and the size of the scanned area.

Findings from the AFM analysis revealed a clear relation between the BCP type and content and the composite roughness. However, it is important to highlight the effect of samples' preparation on their surface roughness. Indeed, sample preparation can be critical and adequate protocol should be considered to eliminate further variation of the surface properties of the film composites. Some examples of defects that can originate from the preparation process are the presence of non-solubilized polymeric crystals, the occurrence of frequent agglomeration of the filler particles due to non-convenient mixing, the formation of air bubbles on the film's surface during curing, etc.

3.2. Nanoindentation analysis

Results of the calculated hardness (H) and Young's modulus (E) of the film composites are summarized in Table 3.

The pure PVA sample had the lowest resistance against indentation load and the highest maximum indentation depth reflected by the lowest H and E values (331 ± 1 MPa and 0.3 ± 0.0 GPa, respectively) among all other samples. In comparison to PVA films, the results from the Tukey-Kramer analysis indicated that there was a statistically significant difference in average H and E in all films except for Y6. These results demonstrate that the addition of BCP improved the overall micro-mechanical features of the composite films. Prior research [36] determined E on the crystalline and amorphous regions of PVA films using nanoindentation, and they reported higher E values compared to our result (24 ± 4.2 GPa and 11.4 ± 3.1 GPa for crystalline and amorphous areas, respectively). This difference can be attributed to the semi-crystalline character of PVA polymer, and E values might differ notably on the surface of the same sample depending on the nature of the region where the indenter's tip was positioned during the test. The shape and dimensions of the utilized probe can also influence the nanoindentation test outcomes, which is another reason to justify the divergence of our result compared to the literature. Moreover, E results can be heavily influenced by the measurement type (i.e., micro-scale or macro-scale). For instance, Mousa and Dong [37] reported 2.08 GPa for E of bulk PVA tested at the macroscopic level by tensile test (ASTM D882-02).

Overall, the micro-mechanical properties of all samples were improved by adding BCP of different types and concentrations. These results are most likely related to both the BCP physio-chemical compositions and porous structure of the BCP particles, which enables strong mechanical adhesion between the fillers and the PVA matrices after the penetration of polymeric molecules inside the BCP pores. Thus, the efficient physical bonding at the PVA/BCP interface likely enhanced the micro-mechanical performance of the composites. The best micro-mechanical properties were achieved by the incorporation of 12 wt%

Table 3
Micro-mechanical properties of PVA and PVA/BCP films.

Samples	Hardness, MPa		Young's modulus, GPa	
	Results	Statistically different from groups[a]	Results	Statistically different from groups[a]
Pure PVA	331 ± 1	All except Y6	0.3 ± 0.0	All except Y6
R-6%	1034 ± 11	W6, Y6	1.0 ± 0.1	W6, Y6
W-6%	568 ± 9	R6	0.7 ± 0.1	R6, Y6
Y-6%	425 ± 10	R6	0.3 ± 0.1	R6, W6
R-8%	2203 ± 14	W8, Y8	1.2 ± 0.1	W8
W-8%	852 ± 14	R8	0.9 ± 0.1	R8, Y8
Y-8%	997 ± 12	R8	1.1 ± 0.1	W8
R-10 %	2933 ± 16	W10, Y10	1.4 ± 0.1	W10, Y10
W-10 %	1024 ± 18	R10	1.1 ± 0.1	R10
Y-10 %	880 ± 15	R10	1.1 ± 0.1	R10
R-12 %	5457 ± 21	W10, Y10	1.8 ± 0.1	W12, Y12
W-12 %	1452 ± 21	R12, Y12	1.5 ± 0.2	R12
Y-12 %	2446 ± 19	R12, W12	1.4 ± 0.1	R12
R-20 %	3641 ± 22	W20, Y20	1.2 ± 0.1	W20
W-20 %	1230 ± 25	R20, Y20	1.3 ± 0.2	R20, Y20
Y-20 %	1015 ± 21	R20, W20	1.1 ± 0.2	W20

[a] Statistically significant differences represent those differences in films within a percent loading, not when comparing films with different loading levels.

BCP where H increased by 1549 %, 339 %, and 639 %, and E increased by 500 %, 400 %, and 367 % by using red oak, willow SV1, and yellow-poplar-derived BCP, respectively.

When analyzing the samples without the influence of BCP content, the results of the Tukey-Kramer analysis indicated that there was a statistically significant difference in average H within every level of BCP loading. A similar pattern appeared in the composite films loaded with 6 wt%, 8 wt%, and 10 wt%. Specifically, within each loading level, films loaded with red oak BCP had a statistically significant higher average hardness than those loaded with willow SV1 and yellow-poplar BCP. Additionally, there was no statistically significant difference in average H between the films loaded with willow SV1 and yellow-poplar BCP within the loading levels of 6 wt%, 8 wt%, and 10 wt%. When the loading level was increased to 12 wt% and 20 wt%, there was a statistically significant difference in average H between BCP produced from all the species. In each case, BCP produced from red oak resulted in the highest average H within each group of loading levels. In the case of 12 wt% loading, the films with yellow-poplar BCP resulted in a higher average H than those loaded with willow SV1 BCP. However, when loading was increased to 20 wt%, the films with willow SV1 BC resulted in a higher average H than those loaded with yellow-poplar BCP.

The higher potential of red oak BCP in enhancing the micro-mechanical performance of the films is likely due to the different physio-chemical compositions, as shown by the proximate analysis results (Table 1), particularly the elevated fixed carbon (93.7 %) and low ash (0.9 %) contents. Additionally, due to the higher carbon content, the red oak BCP had a higher density (0.20 g/cm^3) as compared to the willow (0.14 g/cm^3) and yellow-poplar (0.12 g/cm^3) BCP. However, there was no specific trend in relation to BET surface area, as the red oak, with the highest H value, did not have the highest BET surface area. Specifically, the BET surface area of the red oak BCP was 428.2 m^2/g, as compared to 634.3 m^2/g and 526.4 m^2/g for yellow-poplar and willow, respectively. High carbon content is favorable when using BCP as a filler. Indeed, carbon atoms favor the strong physical bonding with the polymeric matrix chains, leading to increasing the mechanical strength of the composites [15]. Willow SV1-derived BCP contributed less to the enhancement of H when added at different levels compared to red oak and yellow-poplar-derived BCP, which is likely due to the lower carbon content (85.3 %) and higher ash content (4.7 %) that did not enable proper bonding at the filler-matrix interface. When using BCP for filling composites, ash components are considered impurities. Therefore, the occurrence of ash components limited the formation of a continuous carbon-polymer network and resulted in films with lower nano-mechanical features compared to those reinforced with red oak and yellow-poplar BCP (0.9 % and 1.7 % of ash, respectively). In this context, Elnour et al. [38] studied the effect of carbonization temperature on hardwood biocarbon composition and the potential for polyethylene composites reinforcement (20 wt% BC), and they reported that when the pyrolysis temperature increased from 300 °C to 700 °C, the carbon content increased from 63.65 ± 4.44 % to 72.76 ± 1.95 %, and consequently the tensile strength of the composites increased from 30.36 ± 0.08 MPa to 31.87 ± 0.21 MPa. The lower performance of Willow SV1-derived BCP in enhancing the composites' hardness compared to other biomasses could also be related to the large particle size (mean size 495.1 μm), which has likely affected the extent of particle dispersion within the polymeric matrix and consequently led to lower mechanical potential. In a previous study leading to this hypothesis, Vinayagamoorthy [39] studied the effect of limestone particle size (200, 400, 600, 800, and 1000 μm) on the mechanical properties of jute-polypropylene composites and reported that the sample filled with 200 μm particles exhibited higher mechanical properties as compared to the samples filled with bigger particles and that the H of the composites decreased gradually (up to 20 % decrement) with the increase of filler's particle size. Similarly, Abdulkareem et al. [40] stated that the H of polystyrene composites filled with metallic particles (aluminum and iron) was reduced by 428 % when the particle size increased from 20 to 100 μm, which was attributed to the uniform repartition of small size particles.

The results of the Tukey-Kramer analysis showed that there were statistically significant differences in the average E between the sample groups with the same BCP content. Within 6 wt% of BCP loading, there was a statistically significant difference in the average E of the films reinforced with BCP derived from the different species. Specifically, there was a statistically significant decrease in the average E of the films filled with red oak, willow SV1, and yellow-poplar BCP, respectively.

Within BCP loading levels of 10 wt% and 12 wt%, films filled with red oak-derived BCP had a statistically significant higher average E. In addition, there was no statistically significant difference found in average E between the samples filled with willow SV1 and yellow-poplar-derived BCP. However, within BCP loading levels 8 wt% and 20 wt%, films containing willow SV1-derived BCP had a statistically significant difference in average E compared to films containing red oak and yellow-poplar-derived BCP. Further addition of BCP (20 wt%) resulted in a decrement of H and E values. However, they were still much higher than those of pure PVA. This reduction in the micro-mechanical features is most likely related to the occurrence of more BCP aggregates that were grouped randomly in some areas of the films' surfaces. Therefore, there was a higher possibility that the indenter tip hit areas with low BCP concentrations.

Overall, BCP showed good potential for PVA reinforcement. Our results indicate that BCP with high carbon content, low ash content, and

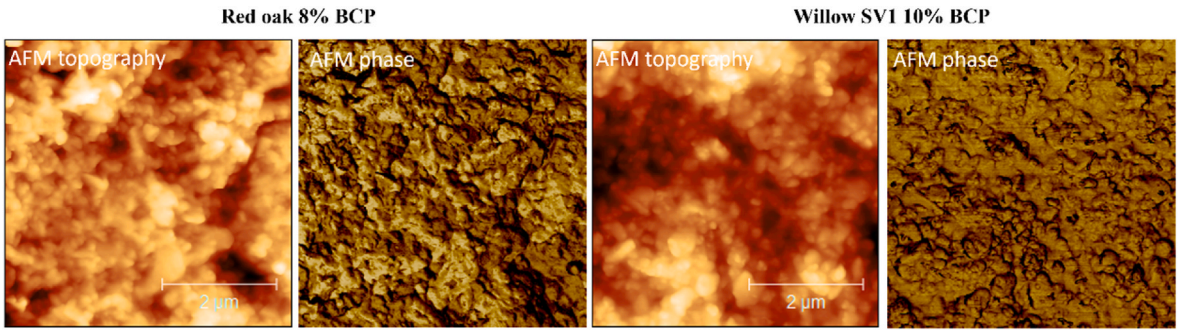

Fig. 2. Exemplary AFM topography and phase images collected on Red Oak and Willow SV1 samples prepared with different BCP concentrations.

small particle size favors achieving better micro-mechanical properties. However, further studies on optimizing the BCP content and ensuring the homogeneous dispersion of the particles inside the polymeric matrix represent an important topic to be explored in future work.

3.3. *Perspectives for future work*

In addition to topographic AFM and nanoindentation data, in our performed experiments, we have also recorded AFM phase images, Fig. 2, which reflect the phase lag between the signal that drives the cantilever oscillation and its output signal. While AFM phase imaging is widely acknowledged as a highly useful tool for polymer microphase separation [41–43] and as a useful means to assess the relative elasticity [44,45] (e.g., assess variations in elasticity across an imaged region of interest), quantitative mechanical mapping is not possible with conventional phase imaging as the phase signal is related to the energy dissipation of the tapping tip which cannot be directly translated into the variation of mechanical moduli [46–48]. An objective of our future planned work stands in combining nanoindentation and topographic AFM data with phase images collected by AFM and by scattering-type Scanning Near-Field Optical Microscopy [49,50] to provide a correlative view that can facilitate a better understanding of the interrelationships that occur between the mechanical properties and the sample's chemical structure. Meanwhile, we provide the AFM phase images collected in our current experiment, next to the topographic AFM and nanoindentation data, as a public resource meant to facilitate community efforts devoted to the in-tandem analysis of AFM topographic and phase data [https://osf.io/kb2u9/?view_only=b81e7ad4b88d4d0d96d47b16ea53bbcd].

4. Conclusion

This study's results showed that both the loading percentage and type of BCP influenced the topography and micro-mechanical performance of the PVA/BCP thin films.

The collected AFM images showed a non-uniform topography characterized by the presence of peaks and valleys. The fluctuation in skewness and kurtosis values also confirmed this non-uniform topography. The average surface roughness increased proportionally with the increase of willow SV1-derived BCP percentage. Roughness changed anomalously when red oak and yellow-poplar-derived BCP were used, attributed to the differences in carbon and ash content and particle size distribution of the three different BCP types. In future work, we plan to implement a similar study using BCP of different origins but with a similar size to shed light on an aspect that remains not well explained. The nanoindentation test showed that by introducing BCP, the hardness and Young's modulus of the films improved dramatically as compared to the neat PVA. The most significant enhancement was achieved with 12 wt% BCP regardless of the original biomass type. However, red oak-derived BCP had the highest potential to enhance the micro-mechanical features, which was attributed to the high carbon content and low ash content as compared to BC prepared from willow SV1 and yellow-poplar. Therefore, PVA film reinforced with 12 % red oak BCP can be a potential composite for packaging applications.

Credit authorship contribution statement

The manuscript was prepared through the contributions of all authors. Mariem Zouari, Stefan G. Stanciu, and David B. DeVallance designed the performed work; Mariem Zouari fabricated the studied samples; Mariem Zouari and Efstathios Fiorentis acquired data; All authors analyzed the results and wrote the manuscript. All authors have approved the final version of the manuscript.

Declaration of competing interest

The authors declare the following financial interests/personal relationships which may be considered as potential competing interests: David DeVallance reports financial support was provided by West Virginia University. Mariem Zouari reports administrative support and article publishing charges were provided by InnoRenew CoE and the Slovenian Research Agency and Grant Agency of the Czech Republic through the WEAVE project (22-14942K). Mariem Zouari reports financial support was provided by EU COST ACTION - ESSENCE and the WEAVE project (22-14942K).

Acknowledgements

This research was funded by the European Commission through the InnoRenew project [739574] under the Horizon 2020 WIDESPREAD-2-Teaming program, COST Action CA19118: ESSENCE, the Republic of Slovenia (investment funding from the Republic of Slovenia and the European Regional Development Fund, ARRS infrastructural program [IO-0035] at the University of Primorska, the ForestValue Research Program, the Slovenian Research Agency and Grant Agency of the Czech Republic through the WEAVE project (22-14942K) and the Republic of Slovenia's Ministry of Education, Science and Sport through the BarkBuild project [No C3330-21-252003]: project BarkBuild is supported under the umbrella of ERA-NET cofund ForestValue 773324.

This research also acknowledges the support provided by the USDA/NIFA McIntire-Stennis Program [WVA00116]. Any opinions, findings, conclusions, or recommendations expressed are those of the authors and do not necessarily reflect the view of USDA/NIFA. SGS, EF, and GAS acknowledge the financial support of UEFISCDI Grants *PN*–III–P1-1.1-TE-2019-1339 OPTIGAN and RO–NO–2019-0601 MEDYCONAI.

Appendix A. Supplementary data

Supplementary data to this article can be found online at https://doi.org/10.1016/j.jmrt.2023.10.217.

References

[1] Finch CA. Polyvinyl alcohol: developments. second ed. Chichester; New York; Brisbane: J. Wiley and Sons; 1992.
[2] Herrmann WO, Haehnel W. Process for the preparation of polymerized vinyl alcohol and its derivatives. Ger. Pat. 1924;480866:2.
[3] Aslam M, Kalyar M. Polyvinyl alcohol: a review of research status and use of polyvinyl alcohol based nanocomposites. Polym Eng Sci 2018;58:2119–32. https://doi.org/10.1002/pen.24855.
[4] Wen Y-H, Tsou C-H, de Guzman MR, Huang D, Yu Y-Q, Gao C, et al. Antibacterial nanocomposite films of poly(vinyl alcohol) modified with zinc oxide-doped multiwalled carbon nanotubes as food packaging. Polym Bull 2021;10:1007–27. https://doi.org/10.1007/s00289-021-03666-1.
[5] Gajra B, Pandya S, Vidyasagar G, Rabari H, Dedania R, Rao S. Poly vinyl alcohol hydrogel and its pharmaceutical and biomedical applications: a review. Int J Pharmacol Res 2011;4:20–6.
[6] Dutra JAP, Carvalho SG, Zampirolli ACD, Daltoé RD, Teixeira RM, Careta FP, et al. Papain wound dressings obtained from poly(vinyl alcohol)/calcium alginate blends as new pharmaceutical dosage form: preparation and preliminary evaluation. Eur J Pharm Biopharm 2017;113:11–23. https://doi.org/10.1016/j.ejpb.2016.12.001.
[7] Mohamady Hussein MA, Guler E, Rayaman E, Cam ME, Sahin A, Grinholc M, et al. Dual-drug delivery of Ag-chitosan nanoparticles and phenytoin via core-shell PVA/PCL electrospun nanofibers. Carbohydr Polym 2021;270:118373–87. https://doi.org/10.1016/j.carbpol.2021.118373.
[8] Wang M, Cheng X, Jiang G, Xie J, Cai W, Li J, et al. Preparation and pervaporation performance of PVA membrane with biomimetic modified silica nanoparticles as coating. J Membr Sci 2022;653:120535. https://doi.org/10.1016/j.memsci.2022.120535.
[9] Nan N, DeVallance DB. Development of poly(vinyl alcohol)/wood-derived biochar composites for use in pressure sensor applications. J Mater Sci 2017;52:8247–57. https://doi.org/10.1007/s10853-017-1040-7.
[10] Chen W, Tao X, Xue P, Cheng X. Enhanced mechanical properties and morphological characterizations of poly(vinyl alcohol)–carbon nanotube composite films. Appl Surf Sci 2005;252:1404–9. https://doi.org/10.1016/j.apsusc.2005.02.138.
[11] Moradi M, Mohandesi JA, Haghshenas DF. Mechanical properties of the poly(vinyl alcohol) based nanocomposites at low content of surfactant wrapped graphene sheets. Polymer 2015;60:207–14. https://doi.org/10.1016/j.polymer.2015.01.044.
[12] Nan N, Devallance D, Xie X. The effect of bio-carbon addition on the electrical, mechanical, and thermal properties of polyvinyl alcohol/biochar composites. J Compos Mater 2015;50:1161–8. https://doi.org/10.1177/0021998315589770.
[13] Basu P. Chapter 5 - pyrolysis. In: Basu P, editor. Biomass gasif. Pyrolysis torrefaction. second ed. Boston: Academic Press; 2013. p. 147–76. https://doi.org/10.1016/B978-0-12-396488-5.00005-8.
[14] Supdipta R, Dinesh M, Ondrej M, Méndez A, Toshiki T. Engineered biochar. first ed. Netherlands: Springer; 2022. http://www.lavoisier.eu/books/chemistry/engineered-biochar/description_4710668. [Accessed 6 January 2023].
[15] Aup-Ngoen K, Noipitak M. Effect of carbon-rich biochar on mechanical properties of PLA-biochar composites. Sustain. Chem. Pharm. 2020;15:100204–12. https://doi.org/10.1016/j.scp.2019.100204.
[16] Devallance D, Oporto G, Quigley P. Investigation of hardwood biochar as a replacement for wood flour in wood-polypropylene composites. J Elastomers Plast 2015;48:510–22. https://doi.org/10.1177/0095244315589655.
[17] Zouari M, Devallance DB, Marrot L. Effect of biochar addition on mechanical properties, thermal stability, and water resistance of hemp-polylactic acid (PLA) composites. Materials 2022;15:2271–87. https://doi.org/10.3390/ma15062271.
[18] Mousa M, Dong Y, Davies IJ. Eco-friendly polyvinyl alcohol (PVA)/bamboo charcoal (BC) nanocomposites with superior mechanical and thermal properties. Adv Compos Mater 2018;27:499–509. https://doi.org/10.1080/09243046.2017.1407906.
[19] Ogurtani TO. The orientation dependent electromigration induced healing on the surface cracks and roughness caused by the uniaxial compressive stresses in single crystal metallic thin films. J Appl Phys 2009;106:535–47. https://doi.org/10.1063/1.3211855.
[20] Choudhary S, Sengwa RJ. ZnO nanoparticles dispersed PVA–PVP blend matrix based high performance flexible nanodielectrics for multifunctional microelectronic devices. Curr Appl Phys 2018;18:1041–58. https://doi.org/10.1016/j.cap.2018.05.023.
[21] Rytöluoto I, Gitsas A, Pasanen S, Lahti K. Effect of film structure and morphology on the dielectric breakdown characteristics of cast and biaxially oriented polypropylene films. Eur Polym J 2017;95:606–24. https://doi.org/10.1016/j.eurpolymj.2017.08.051.
[22] Çaycı D, Stanciu SG, Çapan İ, Erdoğan M, Güner B, Hristu R, et al. The influence of the surface morphologies of Langmuir Blodgett (LB) thin films of porphyrins on their gas sensing properties. Sensor Actuator B Chem 2011;158:62–8. https://doi.org/10.1016/j.snb.2011.05.033.
[23] Guen E, Chapuis P-O, Kaur NJ, Klapetek P, Gomès S. Impact of roughness on heat conduction involving nanocontacts. Appl Phys Lett 2021;119:161602. https://doi.org/10.1063/5.0064244.
[24] Hobbs C, Taylor J, Hong S. Effect of surface roughness on fouling of RO and NF membranes during filtration of a high organic surficial groundwater. J Water Supply Res Technol - Aqua 2006;55:559–70. https://doi.org/10.2166/aqua.2006.038.
[25] Xing R, Lyngstadaas SP, Ellingsen JE, Taxt-Lamolle S, Haugen HJ. The influence of surface nanoroughness, texture and chemistry of TiZr implant abutment on oral biofilm accumulation. Clin Oral Implants Res 2015;26:649–56. https://doi.org/10.1111/clr.12354.
[26] Nan N. Development of polyvinyl alcohol/wood-derived carbon thin films: influence of processing parameters on mechanical, thermal, and electrical properties. Graduate dissertation, Davis College of Agriculture, Natural Resources and Design at West Virginia University; 2016. https://doi.org/10.33915/etd.6289.
[27] Nečas D, Klapetek P. Gwyddion: an open-source software for SPM data analysis. Open Phys 2012;10:181–8. https://doi.org/10.2478/s11534-011-0096-2.
[28] Oliver WC, Pharr GM. An improved technique for determining hardness and elastic modulus using load and displacement sensing indentation experiments. J Mater Res 1992;7:1564–83. https://doi.org/10.1557/JMR.1992.1564.
[29] Pharr GM, Oliver WC, Brotzen FR. On the generality of the relationship among contact stiffness, contact area, and elastic modulus during indentation. J Mater Res 2011;7:61–6. https://doi.org/10.1557/JMR.1992.0613.
[30] Fang T-H, Chang W-J. Nanoindentation characteristics on polycarbonate polymer film. Microelectron J 2004;35:595–9. https://doi.org/10.1016/j.mejo.2004.02.004.
[31] Amaya-Roncancio S, Restrepo Parra E, Devia D, Arias Mateus D, Gomez M. Molecular dynamics simulation of nanoindentation in Cr, Al layers and Al/Cr bilayers, using a hard spherical nanoindenter. DYNA Colomb 2014;81:102–7. https://doi.org/10.15446/dyna.v81n186.39190.
[32] Lee J-H, Lee S-S, Chang J-D, Thompson MS, Kang D-J, Park S, et al. A novel method for the accurate evaluation of Poisson's ratio of soft polymer materials. Sci World J 2013:930798–806. https://doi.org/10.1155/2013/930798. 2013.
[33] Ali HE, Khairy Y. Facile synthesis, structure, AFM, thermal, and optical analysis of BiI3/PVAL nanocomposite films for laser CUT-OFF optical devices. Vacuum 2020;180:109640–52. https://doi.org/10.1016/j.vacuum.2020.109640.
[34] Bajpai AK, Bhatt R, Katare R. Atomic force microscopy enabled roughness analysis of nanostructured poly (diaminonaphthalene) doped poly (vinyl alcohol) conducting polymer thin films. Micron 2016;90:12–7. https://doi.org/10.1016/j.micron.2016.07.012.
[35] Voss A, Stark RW, Dietz C. Surface versus volume properties on the nanoscale: elastomeric polypropylene. Macromolecules 2014;47:5236–45. https://doi.org/10.1021/ma500578e.
[36] Mousa M, Dong Y. Elastic behavior of nanophases in polyvinyl alcohol (PVA)/Bamboo charcoal (BC) nanocomposite films. Front. Mater. 2018;5:44–51. https://doi.org/10.3389/fmats.2018.00044.
[37] Mousa M, Dong Y. Strong poly(vinyl alcohol) (PVA)/Bamboo charcoal (BC) nanocomposite films with particle size effect. ACS Sustainable Chem Eng 2018;6:467–79. https://doi.org/10.1021/acssuschemeng.7b02750.
[38] Elnour AY, Alghyamah AA, Shaikh HM, Poulose AM, Al-Zahrani SM, Anis A, et al. Effect of pyrolysis temperature on biochar microstructural evolution, physicochemical characteristics, and its influence on biochar/polypropylene composites. Appl Sci 2019;9:1149–68. https://doi.org/10.3390/app9061149.
[39] Vinayagamoorthy R. Effect of particle sizes on the mechanical behaviour of limestone-reinforced hybrid plastics. Polym Polym Compos 2020;28:410–20. https://doi.org/10.1177/0967391119883163.
[40] Abdulkareem SA, Amosa MK, Adeniyi AG, Magaji MM, Ajibola RA. Effect of metallic fillers on the hardness of polystyrene composites: an experimental investigation. IOP Conf Ser Mater Sci Eng 2019;640:012058. https://doi.org/10.1088/1757-899X/640/1/012058.
[41] Cheng B-X, Gao W-C, Ren X-M, Ouyang X-Y, Zhao Y, Zhao H, et al. A review of microphase separation of polyurethane: characterization and applications. Polym Test 2022;107:107489. https://doi.org/10.1016/j.polymertesting.2022.107489.
[42] Raghavan D, Gu X, Nguyen T, Vanlandingham M, Karim A. Mapping polymer heterogeneity using atomic force microscopy phase imaging and nanoscale indentation. Macromolecules 2000;33. https://doi.org/10.1021/ma991206r.
[43] Mirhosseini MM, Haddadi-Asl V, Jouibari IS. How the soft segment arrangement influences the microphase separation kinetics and mechanical properties of polyurethane block polymers. Mater Res Express 2019;6:085311. https://doi.org/10.1088/2053-1591/ab1d73.
[44] Magonov SN, Elings V, Whangbo M-H. Phase imaging and stiffness in tapping-mode atomic force microscopy. Surf Sci 1997;375:L385–91. https://doi.org/10.1016/S0039-6028(96)01591-9.
[45] Winkler RG, Spatz JP, Sheiko S, Möller M, Reineker P, Marti O. Imaging material properties by resonant tapping-force microscopy: a model investigation. Phys Rev B 1996;54:8908–12. https://doi.org/10.1103/PhysRevB.54.8908.
[46] García R, Tamayo J, Paulo AS. Phase contrast and surface energy hysteresis in tapping mode scanning force microsopy. Surf Interface Anal 1999;27:312–6. https://doi.org/10.1002/(SICI)1096-9918(199905/06)27:5/6<312::AID-SIA496>3.0.CO;2-Y.
[47] Paulo ÁS, García R. Tip-surface forces, amplitude, and energy dissipation in amplitude-modulation (tapping mode) force microscopy. Phys Rev B 2001;64:193411. https://doi.org/10.1103/PhysRevB.64.193411.
[48] Schön P, Bagdi K, Molnár KK, Markus P, Pukánszky B, Vancso GJ. Quantitative mapping of elastic moduli at the nanoscale in phase separated polyurethanes by AFM. Eur Polym J 2011;47:692–8. https://doi.org/10.1016/j.eurpolymj.2010.09.029.
[49] Chen X, Hu D, Mescall R, You G, Basov DN, Dai Q, et al. Modern scattering-type scanning near-field optical microscopy for advanced material research. Adv Mater 2019;31:1804774. https://doi.org/10.1002/adma.201804774.
[50] Kim J, Lee W, Kim H, Ryu DY, Ahn H, Chae B. In-depth probing of thermally-driven phase separation behavior of lamella-forming PS-b-PMMA films by infrared nanoscopy. Spectrochim. Acta. A. Mol. Biomol. Spectrosc. 2022;274:121095. https://doi.org/10.1016/j.saa.2022.121095.